Corrosion testing of materials in simulated superheated geothermal environment

Andri Isak Thorhallsson[a,*], Andri Stefansson[b], Danyil Kovalov[a], Sigrun Nanna Karlsdottir[a]

[a] Faculty of Mechanical Eng., Industrial Eng. and Computer Science, University of Iceland, Hjardarhagi 2-6, 107 Reykjavik, Iceland
[b] Institute of Earth Sciences, University of Iceland, Sturlugata 7, 101 Reykjavik, Iceland

ARTICLE INFO

ABSTRACT

This paper reports the results of corrosion study for carbon steel, austenitic stainless steel, as well as titanium and nickel-based alloys which were tested in a simulated superheated geothermal environment (SSGE) in flow-through reactors to investigate the corrosion behaviour to aid in the future material selection for high temperature deep geothermal application. The testing fluid was superheated steam (T = 350 °C and P = 10 bars gauge) containing H_2S, CO_2 and HCl with condensate of pH = 3. The corrosion rate for all samples was negligible but carbon steel was prone to localized damage under a magnetite film with a sulphur rich sublayer.

1. Introduction

Geothermal fluids formed in the upper part of the Earth's crust associated with active volcanism have been utilized for energy production worldwide. Conventional exploitation of geothermal fluids from such systems typically produces an average of ~3–5 MW electric power per well [1]. The reservoir fluid temperatures of such geothermal systems are typically 230 − 350 °C. However, geothermal fields where temperatures exceed the critical temperature of water have also been reported for several fields in Iceland, Kenya, Italy, USA, Japan and Mexico [2]. Utilization of such fluids has been predicted to increase power production per well of up to ~30 − 50 MW [3]. Utilizing geothermal energy from geothermal wells is important in the renewable energy mixture and drilling deeper geothermal wells can, therefore, potentially increase the power production from each well. At the beginning of the 21st century, a scientific program called the Iceland Deep Drilling Project was founded. The aim of the project was to drill 3.5–5 km deep wells in three geothermal fields in Iceland and extract 450 − 600 °C supercritical fluid to make the geothermal energy output much higher and the operation per well more economical [3]. Supercritical water is where temperatures and pressures are above the critical point of 221.2 bars and 375.15 °C but the supercritical point of H_2O shifts when dissolved components are present in the fluid [4]. For pure water, if enthalpy is higher than the critical enthalpy of 2086 J/g, the steam exists in single phase supercritical condition. Experience from the first deep drilled well of the IDDP, IDDP-1, revealed that the energy output of deep geothermal wells can be an order of magnitude higher

than from a regular high temperature well [5]. The temperature in the IDDP-1 well in Iceland was 450 °C and 140 bars at the wellhead. Gas samples from the steam in IDDP-1 were collected during the discharge of the well and average concentrations recorded for some corrosive species were H_2S = 339 mg/kg, CO_2 = 732 mg/kg, H_2 = 10 mg/kg, Cl = 93 mg/kg, F = 5 mg/kg, NH_3 = 0.14 mg/kg. Other chemical species in the steam were Fe = 8.4 mg/kg, B = 1 mg/kg and the pH of the condensed steam was 2.62 [6]. Due to the high temperature and high pressure conditions met in the IDDP-1 well and future plans for drilling more deep drilling wells, corrosion tests were conducted at the wellhead during the discharge of the IDDP-1 well to gain a better understanding of the corrosion behaviour of materials in high temperature deep geothermal environment. Extensive corrosion testing was conducted in-situ during the discharge of the IDDP-1 well [7–10]. From these corrosion studies, corrosion coupon testing [7] conducted at the wellhead is probably the most significant in-situ study made so far in deep geothermal superheated systems and most relevant for this research. In the in-situ corrosion coupon testing, several alloys (including carbon steel, austenitic stainless steel, duplex steel, nickel-based and titanium alloys) were tested in a pipe connected to the wellhead for a total of 113 days at 350 − 360 °C and 12 − 13 bars pressure. Due to the pressure drop used in the test pipe during testing, amorphous silica supersaturated in the steam and formed heavy silica scaling on the test samples [7]. All the samples in the in-situ coupon test had low corrosion rates, well below 0.01 mm/year where low carbon steel S235JRG2 and nickel-based alloy UNS N06625 had corrosion rates of 0.004 mm/year and 0.001 mm/year respectively [7]. Even though corrosion rates were

low in the in-situ testing, localized corrosion damage was found in all the tested samples. Furthermore, the localized damage was observed under the silica scale and questions arose whether the silica scaling was catalysing corrosion in the samples tested. From the overall corrosion coupon testing in the first deep geothermal well in Iceland, it was concluded that silica scale covering the samples provided protection against general corrosion but possibly promoted localized corrosion under the silica deposits [7]. The corrosive species in the superheated geothermal steam mentioned previously [6] included; CO_2, H_2S, HCl, HF and H_2. It has to be noted here that there were no conclusions on the corrosion effect or contribution of each corrosive species to the localized corrosion of the alloys investigated after the in-situ testing. Eventually, the IDDP-1 well was quenched and closed in 2012 due to operational problems resulting from corrosion in valves [11].

Only a few studies have reported corrosion data in superheated geothermal systems other than the corrosion testing conducted during the discharge of the IDDP-1 well [7–10]. In 1980, corrosion testing was done in well KG-12 in Krafla, Iceland at 7 bars gauge in a 220 °C superheated geothermal fluid containing HCl. All of the alloys, including carbon steel, stainless steel and nickel-based alloys were prone to localized damage except the austenitic stainless-steel UNS S31254 and the nickel-based alloy UNS N06255. The corrosion rate for the carbon steel was approximately 0.3 mm/year in the superheated steam [12] which was an order of magnitude higher than the corrosion rate observed in the in-site testing in IDDP-1 well mentioned above [7]. Due to the high corrosion rate of carbon steel in KG-12 and small superheat of the steam, condensation of the geothermal fluid in the testing pipe was considered to have occurred during the testing in well KG-12. In 2010, down-hole corrosion testing was done for alloys in an acidic, high temperature geothermal well KJ-39 in Krafla Iceland. The temperature was around 293 °C at the wellhead but around 350 °C at the bottom with a pressure range from 13 bar to 20 bar. The pH of the condensate sampled at the wellhead was measured as 4.1. The geothermal fluid contained CO_2, H_2S, HCl, H_2 as well as CH_4 and SO_4. The results of the corrosion testing showed pitting in the carbon steels, the stainless-steel and the nickel-based alloys tested. The corrosion rate reported was very high for the carbon steel and martensitic stainless steel but very low for austenitic stainless steel and the nickel-based alloys or below 0.1 mm/year. From the data gathered and experience in the operation of the KJ-39 well, it was concluded that superheated geothermal fluid from the bottom of well mixed with colder geothermal fluid flowing into the well at lower depth resulting in severe corrosion of the well liner at 1600 m depth [13]. This resulted in acidic conditions in the mixing zone which produced low pH fluid to be in contact with the testing samples in the sour well. The electrochemical study by Bogaerts et al. [14] on stainless steels and nickel-based alloys in relevant environment (chloride rich with some anions) but in aqueous solutions up to 300 °C and 120 bars implies that pitting potential of all the alloys is at a minimum between 150 − 200 °C [14]. These results indicate a link between corrosion behaviour and temperature is not straightforward.

From the studies and diverse results mentioned above, it can be concluded that corrosion behaviour of materials in high temperature, superheated and supercritical geothermal environment has not yet been fully understood. Testing material in-situ in superheated geothermal fluid has not been possible since 2012 or when the first Iceland deep drilling well was quenched and closed. Thus, there is lacking a platform to study the corrosion behaviour of potential candidates of deep geothermal wells, which is crucial for the design of such future wells.

The objective of this work was to study the corrosion behaviour of materials in a simulated superheated geothermal environment at a stable, controlled condition. A testing facility of flow-through reactors was established with a purpose to simulate geothermal high temperature environment that can be encountered in deep geothermal wells. In this paper, we report on the simulated testing done for carbon steel, austenitic stainless-steels, nickel-based alloys and titanium alloy in sequential flow-through reactors containing superheated steam of 350 °C

and at 10 bar gauge containing CO_2, H_2S and HCl as the corrosive species. The aim of the paper was to 1) establish laboratory testing facility that can accommodate testing samples in a superheated steam containing H_2S, CO_2 and HCl from a laboratory-made solution and 2) perform corrosion experiments to understand the corrosion behaviour of carbon steel, austenitic stainless steel, nickel-based alloys and titanium alloy in a controlled simulated superheated geothermal environment.

2. Experimental

2.1. Flow-through reactors testing facility and condition

One of the objectives of this study was to design flow-through reactors testing facility with controlled testing parameters to be able to perform corrosion testing in superheated laboratory prepared fluid that has similar properties as geothermal fluid from a field. Pre-testing trials were done to adjust and optimize the testing conditions, including change in design, flow, insulation and external heating, etc. In the first steps of developing the testing equipment, low grade stainless-steel samples were used for assessing the uniformity in the test conditions. For the 1st generation of the test setup, the design of equipment and set testing parameters resulted in inhomogeneous conditions in the reactors i.e. boiling and condensation of the fluid at inlet and outlet, respectively, in the test volume [15]. Based on the unsatisfactory experimental conditions stated above, additional adjustments of the laboratory equipment and parameters were done. Subsequent to these adjustments, nickel-based alloy samples were tested in the next testing batch, but some localized nickel sulphide deposits were observed on part of the samples indicating non-uniform conditions in the reactor [16]. The non-uniform conditions occurred probably due to cooling effects at inlet and outlet to the reactors and due to transportation of liquid solution due to flashing of liquid from preheater to the reactors when pumps primed during the first pretesting. Further adjustments of the equipment and tuning of process parameters led to homogeneous corrosion behaviour and consistent corrosion rate between all the tested samples within the two reactors indicating more uniform conditions in the reactor volume. To confirm the superheated state of the testing fluid, resistor temperature detector (RTD) with platinum detector was connected between the preheater and the first reactor; between the two reactors and at the outlet of the second reactor. In this paper, the results for testing using the fully developed laboratory facility are reported. Fig. 1 shows a photo of the corrosion testing equipment and Fig. 2 shows the corresponding flow diagram of the flow-through loop equipment.

Two combinations of H_2S and CO_2 concentrations were used in the testing; a lower concentration of H_2S = 30 ppm and CO_2 = 80 ppm, and a higher concentration of H_2S = 150 ppm and CO_2 = 250 ppm. Two solutions were mixed to obtain the H_2S and CO_2 gases for simulating a geothermal steam environment in the tests. The setup and operation of the testing facility can be outlined as follows: two reactant solutions were pumped from two volumetric flasks using Chrom Tech series I pumps. The solutions were degassed by Labhut degassers and then mixed before entering the preheater. The tubing at the inlet of the flow-through loop, from mixing to the inlet of the preheater is made of stainless UNS S31603. The material in the flow-through loop in the hot temperature part of the flow line i.e. in the preheater, the reactors and tubing between the preheater and reactor, a tubing between reactors and tubing between second reactor and pipe at outlet towards condenser was made of corrosion resistant alloy UNS N10276. The sample holder and fasteners were made of Inconel UNS N06625 and UNS S31603 materials of which were used depending on the alloy type of the sample in the testing batch. Washers between samples and fasteners are made of ceramic alumina provided by Ortech. The hot temperature part of the flow-through loop was highly insulated with ceramic material ($SiO_2/Al_2O_3/MgO$) and glass wool to minimize heat loss. The preheater,
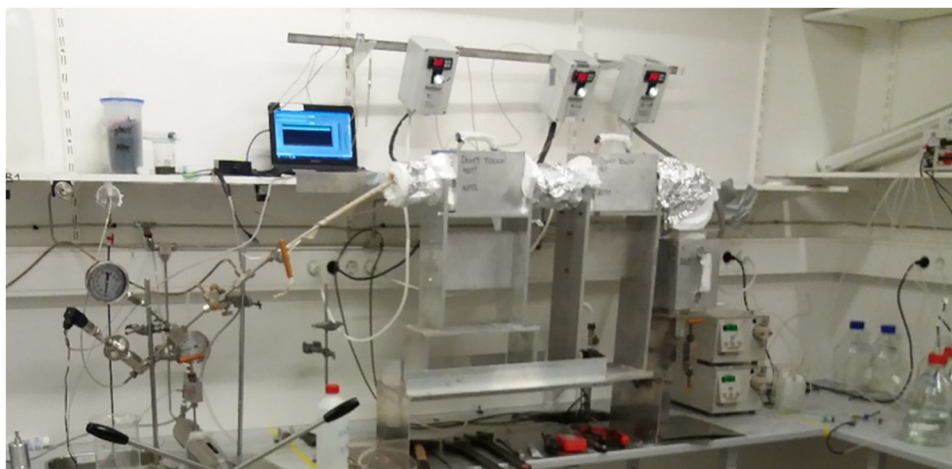
Fig. 1. Corrosion testing equipment setup.

reactors, and heating units were custom made. The temperature of the reactors was regulated by a temperature controller and elements from Rafhitun. Thermocouples used in the system were connected to the reactor pipes externally. Another set of thermocouples were connected to the reactor pipes externally to the Labjack U6 series data logger. All thermocouples connected to the heating units are K-type. Stainless steel and nickel-based alloy tubing, fittings and condenser were provided by SITEC. The piping at the outlet of the second reactor was wrapped with HTS Amptek heating tape. Analog pressure meter was connected to the flow line after the condenser. Digital pressure transducer, WIKA model S-20, was connected to the Labjack U6 datalogger to monitor the pressure in the flow-through loop system. The back pressure regulator (BPR) was designed and custom made by Prologo to set and control fluid pressure in the system. The external pressure controller exerting on the BPR was a SITEC 750 hand pump.

The initial plan was to run a 21-day testing period for all the testing batches at low and high concentration. At a higher concentration of H_2S and CO_2, deposits accumulated at the condensing part of the experiment that led to a slow build-up of pressure inside the system, after approximately two weeks of testing. As a result, the testing period at higher concentration was decided to be limited to 10 days. Testing periods and main parameters for all the materials tested are shown in Table 1.

Before each run of the test batches, the process volume was flushed with deionized water at room temperature for 24 h to remove air in the system. The system volume was then heated up to 350 °C at 10 bars with pure steam to stabilize the system before the testing fluid was injected into the flow-through loop. At the end of each testing batch experiment, testing fluid was flushed with pure steam before the pre-heater and reactor temperature was lowered to ambient temperature. This procedure was done to prevent acidic condensation in the reactor volume during shut down of experiment. The stability of pressure within the system was ± 0.5 bar and stability of preheater and reactors was ± 2 °C.

2.2. Testing fluid

The testing fluid was a mixture of two aqueous solutions, whereas the first solution contained HCl while the second solution contained anhydrous Na_2S and $NaHCO_3$. Anhydrous Na_2S and $NaHCO_3$ were weighted in deionized water solution to get the target concentrations of H_2S and CO_2 in the final corrosion testing solution. The chemical reactions between Na_2S and HCl, and $NaHCO_3$ and HCl when the reactant solutions were mixed were as follows:

$$Na_2S + 2HCl = H_2S + 2NaCl \tag{1}$$

$$NaHCO_3 + HCl = CO_2 + H_2O + NaCl \tag{2}$$
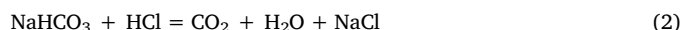
The sulphide $[S^{2-}]$, hence the H_2S, and CO_2 concentration in the reactant solutions were verified and titrated after preparation of the reactant solutions. To determine S^{2-} concentration in the $Na_2S/NaHCO_3$ reactant solution, 5 ml of acetone and 5 ml of 5 M NaOH were mixed into mixing flask. A 0.2 ml of the $Na_2S/NaHCO_3$ solution was
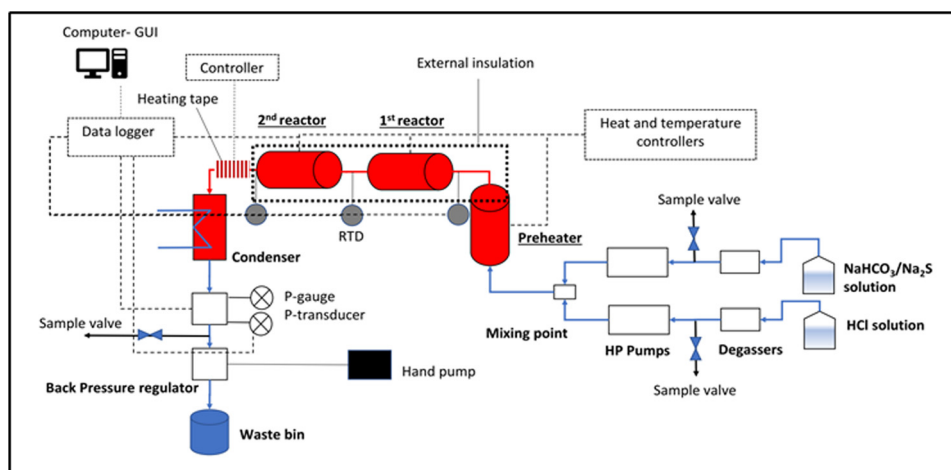

Fig. 2. Corrosion testing flow diagram.

Table 1
Materials tested and main parameters in test batches.

Test batch no.	Material type	Alloy	Test period [Days]	Inlet volumetric flow [ml/min]	Fluid gauge pressure [bar]	Fluid temperature [°C]	H_2S [mg/kg]	CO_2 [mg/kg]
1	Ni-based alloys	UNS N06255	21	0.3	10	350	30	80
2[a]		UNS N06845	16	0.3	10	350	30	80
3		UNS N06625	21	0.3	10	350	30	80
4	Carbon steel	S235JRG2	10	0.3	10	350	150	250
5	Aust. St. steel	UNS S31254	10	0.3	10	350	150	250
6		UNS S31277	10	0.3	10	350	150	250
7	Ni-based alloys	UNS N06625	10	0.3	10	350	150	250
8		UNS N06845	10	0.3	10	350	150	250
9	Ti-based alloy	Ti-4Al-4Mo-2Sn	10	0.3	10	350	150	250

[a] Stopped at 16th day due to leakage at fitting.

added to the mixing flask with a precise and calibrated micropipette. Afterwards, 40 ml of deionized water was poured into the Erlenmeyer flask and then trace amount of dithizone crystals was added to the total solution until turned pale yellow. The total solution in the Erlenmeyer flask was then titrated with 0.001 M Hg-acetate solution until the colour of the total solution changed to pale pink, indicating that all sulphide ions were reacted with mercury ions. When mercury acetate is used to titrate the sulphur ions, where mercury cations react with the sulphur anions in the solution according to

$$Hg^{2+} + S^{2-} -> HgS \tag{3}$$
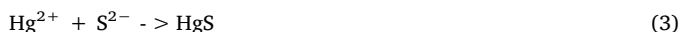
When all the sulphur anions S^{2-} have reacted in the solution, the mercury cations start to react with dithizone ($C_{13}H_{12}N_4S$) and the colour of solution changes to pink [17]. To determine the concentration of the CO_2 in the solution, the equilibrium of CO_2 with carbonic acid, bicarbonate and carbonate was considered [18,19] according to equilibrium in:

$$CO_2 + H_2O = H_2CO_3 \tag{4}$$

$$H_2CO_3 = HCO_3^- + H^+ \tag{5}$$

$$HCO_3^- = CO_3^{2-} + H^+ \tag{6}$$

The carbonic acid is a weak acid, hence the left side of reaction (4) is dominant at low pH (< 4.5). Furthermore, the dissolved CO_2 in the solution is volatile at low pH with a tendency to degas from the solution. To determine the CO_2 concentration in the $Na_2S/NaHCO_3$ reactant solution, a known volume of the reactant solution was titrated with Metrohm 765 Dosimat (with Metrohm 780 pH meter calibrated with standardized pH = 4.00 and 7.00 solutions) until the solution pH was 8.3 with 0.1 M HCl solution. Subsequently, the solution was further titrated with 0.1 M HCl until pH = 4.5. The solution was then degassed for at least 15 min with bubbling inert N_2 gas until CO_2 and H_2S were eliminated from the solution. The solution was set again to pH = 4.5 with the 0.1 M HCl. The solution was then back titrated with 0.1 M NaOH solution until pH = 8.3. From the amount of HCl and NaOH used in titration and back-titration and from the known concentration of H_2S in the solution, the CO_2 could be determined (Table 2).

During corrosion tests, the flow rate and pH of the fluid condensate at the outlet were regularly measured as well as the titration of H_2S and CO_2 of the fluid were done at the outlet. In order to conduct the titration of the outlet fluid, H_2S and CO_2 gases were to be extracted with 0.1 M NaOH solution to avoid the escape of the gases from the fluid. The waste fluid was eventually accumulated in a waste bin containing the solution of NaOH with Zn-acetate to neutralize the H_2S gas.

The chemical composition of the testing fluid for simulating high temperature geothermal fluid with two different concentration of H_2S and CO_2 is given in Table 3. A comparison of the physical and chemical properties of the two testing fluids in the simulated testing to IDDP-1 fluid is also shown in Table 3. The testing in simulated geothermal environment were done at two different concentrations of H_2S and CO_2

Table 2
Number of moles of the chemical species and total volume of the reactant solutions at low and high concentration of H_2S and CO_2 in the mixed solution.

Parameter	Simulated testing - low concentration	Simulated testing - high concentration	Unit
Reactant solution no. 1			
HCl	9.2	31	mmol
Total volume	1000	1000	ml
Reactant solution no. 2			
Na_2S	1.8	8.8	mmol
$NaHCO_3$	3.6	11.4	mmol
Total volume	1000	1000	ml

Table 3
Comparison between fluid properties in simulated testing vs. previous in-situ testing in Iceland Deep Geothermal Well no. 1 [9].

Parameter	Simulated testing - low concentration	Simulated testing - high concentration	In-situ testing IDDP-1	Unit
pH	3.0	3.0	2.62	
Temperature	350	350	350 – 360	°C
Fluid pressure	10	10	12 – 13	bar
Fluid velocity	0.012	0.012	2 – 5	m/s
Testing period	21[a]	10	113	Days
Cl	35.5[b]	35.5[b]	93	mg/kg
CO_2	80	250	732	mg/kg
H_2S	30	150	339	mg/kg
H_2	–	–	10	mg/kg
F	–	–	5	mg/kg

[a] UNS N06226 tested in 16 days.
[b] From pH = 3.

in laboratory; low concentration (H_2S = 30 mg/kg and CO_2 = 80 mg/kg) and high concentration ((H_2S = 150 mg/kg and CO_2 = 250 mg/kg).

2.3. Testing materials

The types of materials tested included carbon steel (S235JRG2), two types of austenitic stainless-steels (UNS S31254 and S31277) and three nickel-based alloys (UNS N06255, N06625 and N06845) and one titanium alloy grade (Ti-4Al-4Mo-2Sn). Three flat coupon samples of each material were tested in each testing batch. Two of the coupons had dimensions 100 mm x 7 mm x 1 − 2 mm for weight loss analysis and one coupon for microstructural and chemical composition analysis of the cross-section had a dimension of 100 mm x 7 mm x 1 − 2 mm. The thickness of the coupons for each material depended on their availability from the producers. The nickel-based alloys were the only material tested in the low concentrations of H_2S and CO_2. Overview of the

Table 4
Chemical composition (main elements) of the alloys tested in the simulated corrosion testing.

Material	UNS number	Other designation	Nominal composition [% wt]												
			C	Si	Mn	Cr	Ni	Mo	Cu	Al	Nb	Ti	W	Sn	Fe
Carbon steel	N/A	NS-EN S235JRG2 (ASTM A 284C)	0.04	0.02	0.20	0.04	0.02	0.00	0.040	0.04	0.00	0.00			bal.
Austenitic stainless steel	S31254		0.02[a]	0.8[a]	1.0[a]	20.0	18.0	6.1	0.7						bal.
	S31277		0.02[a]	0.5[a]	3.0[a]	23[a]	28[a]	8[a]	1.5[a]						bal.
Nickel-based alloy	N06255		0.03[a]	1.0[a]	1.0[a]	26[a]	52[a]	9[a]	1.2[a]				3[a]		bal.
	N06845		0.05[a]	0.5[a]	0.5[a]	25[a]	50[a]	7[a]	4[a]				5[a]		bal.
	N06625		0.1[a]	0.5[a]	0.5[a]	23[a]	58.0[b]	10[a]		0.4[a]	4.15[a,c]	0.4[a]			5.0[a]
Titanium alloy	N/A	Ti-4Al-4Mo-2Sn		0.7[a]				5[a]		5[a]		bal.		2.5[a]	0.2[a]

[a] Maximum value.
[b] Minimum value.
[c] Nb + Ta.

materials and their chemical composition is given in Table 4.

2.4. Sample preparation and geometry

All the samples were ground to 600 grit with SiC abrasive paper before corrosion testing. The samples were then cleaned in ethanol and ultrasound bath and weighed and measured according to ASTM G1-90 before corrosion testing. The measured corrosion rate (CR) of the material tested in mm/year was calculated via the weight loss method and according to standard [20]:

$$CR = \frac{K \cdot W}{A \cdot t \cdot \rho} \qquad (7)$$

Where K is the corrosion rate constant equal to $8.76 \cdot 10^4$ mm/year, W is the mass loss in grams of the tested material with a ± 0.00005 g precision, A is the exposed surface area in cm^2 of a tested sample, t is the exposure time in hours, and ρ is the material density in g/cm^3.

2.5. Post exposure measurements and analysis

For weight loss analysis, the samples were cleaned to remove corrosion products according to ASTM G1-90. It is to be noted here that there is no standard cleaning procedure available for Ti-based alloys due to extreme adhering titanium oxide film. Therefore, the Ti-based alloy in the experiment was only cleaned by ethanol in the ultrasonic bath after testing. For Scanning Electron Microscope (SEM), X-ray Electron Dispersive Spectroscope (XEDS) and grain boundary analysis, the samples applied for microstructural analysis were sectioned using a diamond wafering blade, mounted in thermosetting phenol formaldehyde resin (i.e., bakelite) and cast under pressure. The samples were ground to 1000 grit with SiC abrasive paper and polished with 3 μm and 1 μm diamond paste slurry and 0.02-0.06 μm particle size colloidal silica. The samples were analysed using SEM and XEDS before and after the corrosion testing. The SEM equipment used was a Zeiss Supra 25. The XEDS instrument used is Oxford Instruments with Si(Li) X-ray detector and INCA Energy 300 software. For grain boundary analysis, 2% nital [21] was used for etching of carbon steel S235JRG2. Kroll's reagent [22] was used for etching of alloy Ti-4Al-4Mo-2Sn. Mixed acids [23] were used for etching of the nickel-based alloys and the austenitic stainless-steels. The grain boundary analysis was done using Meiji Techno's MT7530OH optical microscope with Infinity Analyze software. The corrosion rate was determined via the weight loss method. The microstructure and corrosion forms of the samples were analysed using SEM. The chemical analysis was done by XEDS. The crystal structure of the materials was analysed in-situ by X-Ray Diffractometer (XRD) before and after corrosion tests with XPert Pro XRD meter from PANalytical with Data Collector software.

3. Results

3.1. Weight loss analysis

The weight loss method was applied to determine the corrosion rate of the tested samples. The corrosion rate for all the tested materials, at low and high concentration of H_2S and CO_2, was low, as shown in Fig. 3. The corrosion rates of nickel-based alloys tested in a low concentration of H_2S = 30 mg/kg and CO_2 = 80 mg/kg were in the order of 0.001 mm/year for all three nickel-based alloys tested. The corrosion rate of the nickel-based alloys UNS N06625 and N06845 in the higher concentration environment was comparable to the corrosion rate observed for the nickel-based alloys in the lower concentration testing. The corrosion rates of the austenitic stainless steels UNS S31254 and S31277 were higher than for the nickel-based alloys. No weight loss was measured for the titanium alloy Ti-4Al-4Mo-2Sn but negligible weight gain was observed with a negative corrosion rate value of -0.005 mm/year (presented as 0 mm/year in Fig. 3). The measured corrosion rate of the carbon steel S235JRG2 was low, 0.042 mm/year, but one to two orders of magnitude higher than the corrosion rate in comparison with the corrosion resistant alloys.

3.2. Microstructural and chemical analysis

3.2.1. Low Concentration, H_2S = 30 mg/kg and CO_2 = 80 mg/kg

Negligible corrosion film and no form of localized corrosion damage were observed in the nickel-based alloys in the SEM and XEDS analysis after tests at H_2S = 30 mg/kg and CO_2 = 80 mg/kg shown in Fig. 4. Titanium and niobium enriched nitrides were detected in blank and exposed samples of UNS N06625. A small amount of sulphur was detected at the surface on all the nickel-based alloys tested but were not easily detected in cross-section analysis as can be seen from the XEDS results in the table in Fig. 4.

3.2.2. Higher Concentration, H_2S = 150 mg/kg and CO_2 = 250 mg/kg

SEM images of the cross-sectional analysis of the austenitic stainless-steels are shown in Fig. 5 and for the nickel-based alloys and the titanium alloy in Figs. 6 and 7, respectively. Figs. 8 and 9 show SEM images of the cross-sectional and surface analysis of the carbon steel. Crystalline magnetite surface film formed on the surface of carbon steel after the corrosion testing as shown in Fig. 9. The XEDS analysis of the area shown in Fig. 10 indicates that this was likely magnetite crystals, Fe_3O_4, that have formed during the testing. The more corrosion resistant alloys i.e. the austenitic stainless-steels, nickel-based alloys and the titanium alloy were not susceptible to any localized corrosion damages in the simulated geothermal environment. No indication of pitting or cracking was observed in the austenitic stainless-steels, nickel-based alloys or the titanium-based alloy. In general, only small traces of sulphur were detected on the surface of the corrosion resistant alloys. The low carbon steel, however, had approximately 10 μm thick film

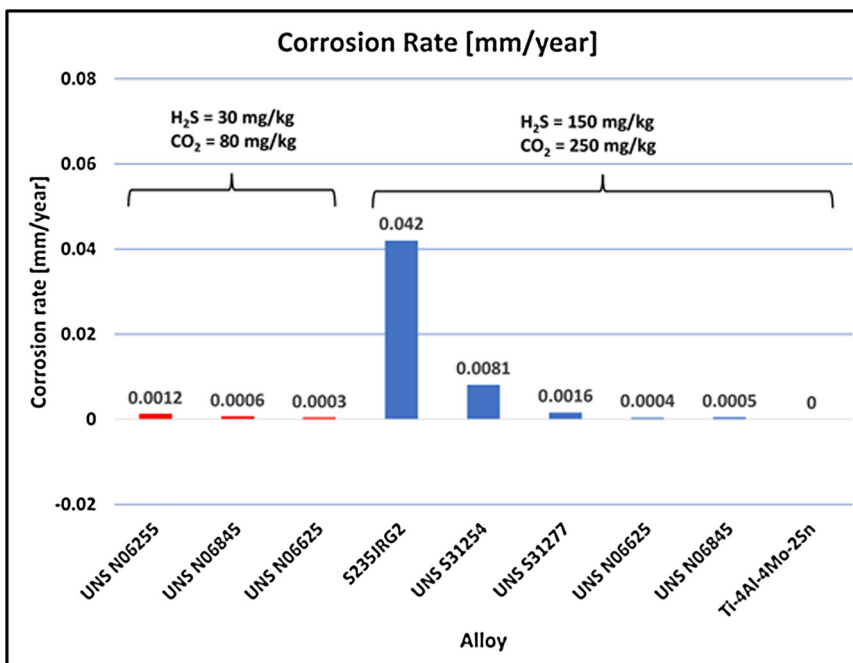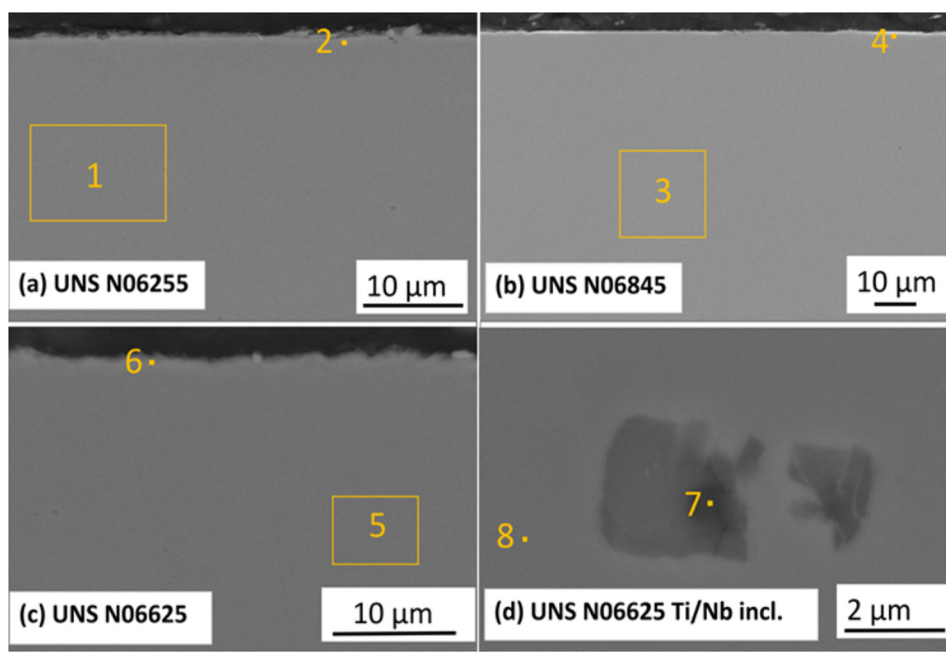**Fig. 3.** Corrosion rate in low ($H_2S = 30$ mg/kg, $CO_2 = 80$ mg/kg) and high ($H_2S = 150$ mg/kg, $CO_2 = 250$ mg/kg).

Location	N	O	Mg	Al	S	Si	Ti	Cr	Mn	Fe	Ni	Nb	Cu	Mo	W
1	-	-	-	-	-	0.4	-	24.5	0.8	19.3	47.9	-	0.6	6.2	0.4
2	-	1.7	-	-	-	0.5	-	21.9	0.7	19.1	50.0	-	0.5	5.5	0.2
3	-	-	-	-	-	-	-	22.9	-	16.4	47.4	-	3.0	6.0	4.4
4	-	6.1	-	-	0.3	-	-	19.8	-	15.3	44.7	-	2.7	5.2	5.9
5	-	-	-	-	-	-	0.3	22.4	-	3.3	61.7	3.5	-	8.8	-
6	-	-	-	1.7	-	1.6	0.3	19.5	-	3.8	60.9	3.1	-	9.1	-
7	4.5	4.1	15.8	-	-	-	41.2	7.0	-	0.9	14.9	9.8	-	1.9	-
8	-	-	-	-	-	-	0.2	22.3	-	3.4	61.9	3.1	-	9.1	-

Fig. 4. SEM cross section images and XEDS analysis of testing materials in $H_2S = 30$ mg/kg and $CO_2 = 80$ mg/kg (a) UNS N06255, (b) UNS N06845, (c) UNS N06625 and (d) Ti/Nb rich inclusions in UNS N06625.
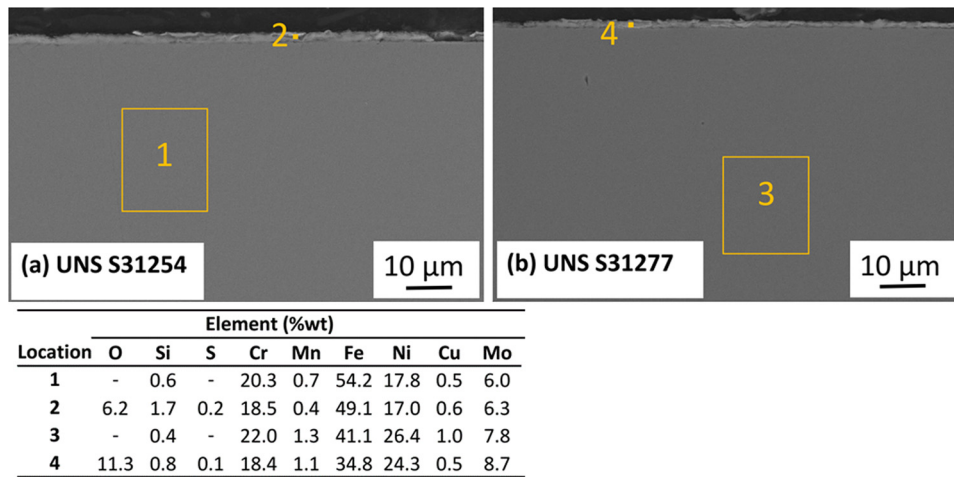
	Element (%wt)								
Location	O	Si	S	Cr	Mn	Fe	Ni	Cu	Mo
1	-	0.6	-	20.3	0.7	54.2	17.8	0.5	6.0
2	6.2	1.7	0.2	18.5	0.4	49.1	17.0	0.6	6.3
3	-	0.4	-	22.0	1.3	41.1	26.4	1.0	7.8
4	11.3	0.8	0.1	18.4	1.1	34.8	24.3	0.5	8.7

Fig. 5. SEM cross section images and XEDS analysis of austenitic stainless steels (a) UNS S31254 and (b) UNS S31277 in $H_2S = 150$ mg/kg and $CO_2 = 250$ mg/kg.

rich in oxygen and iron indicating the presence of Fe_3O_4, magnetite layer on the surface. Between the thick outermost layer and the bulk material, a thinner sulphur rich film was observed. Furthermore, chloride rich pits were distributed under the magnetite and sulphur layers as can be seen in Fig. 10. From the deepest pit observed it was concluded that the maximum pit penetration rate was approximately 0.4 mm/year.

3.3. XRD analysis

X-Ray Diffraction (XRD) analysis was done for all the corroded and blank samples to study morphology and formation of new crystalline phases on the surface after the testing. No significant difference was observed between XRD graphs for the nickel-based alloys in low concentration of H_2S and CO_2 as seen in Fig. 11. This was also the case for the nickel-based alloys at the higher concentration of H_2S and CO_2, but small magnetite peaks were detected in the austenitic stainless-steels as seen in Fig. 12. The α-phase in the titanium alloy Ti-4Al-4Mo-2Sn was analysed but in essence, no new crystalline phases were observed after corrosion testing as seen in Fig. 13. For the carbon steel tested, however, magnetite crystals of Fe_3O_4 formed on the surface which is consistent with the XEDS analysis. The XRD graphs of the un-tested and corrosion tested carbon steel are given in Fig. 14. This result implies that the hot steam is oxidizing the iron surface of the carbon steel according to Eqs. (1) and (2) in Cotton [32] and Evans [33], respectively as described in the Discussion chapter.
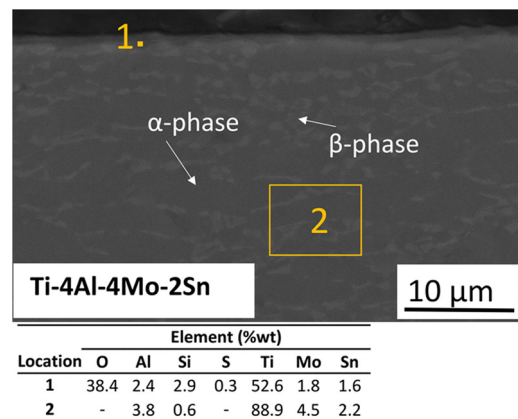

	Element (%wt)						
Location	O	Al	Si	S	Ti	Mo	Sn
1	38.4	2.4	2.9	0.3	52.6	1.8	1.6
2	-	3.8	0.6	-	88.9	4.5	2.2

Fig. 7. SEM image of a cross section and XEDS analysis of titanium alloy Ti-4Al-4Mo-2Sn in $H_2S = 150$ mg/kg and $CO_2 = 250$ mg/kg.

3.4. Microetching

Microetching of all the tested samples was done to determine if intergranular corrosion could be observed after the corrosion testing and because of previous experience from in-site testing in IDDP-1 [7]. No grain boundary defects were however observed in the samples but localized damage (pitting) was observed under the surface of the
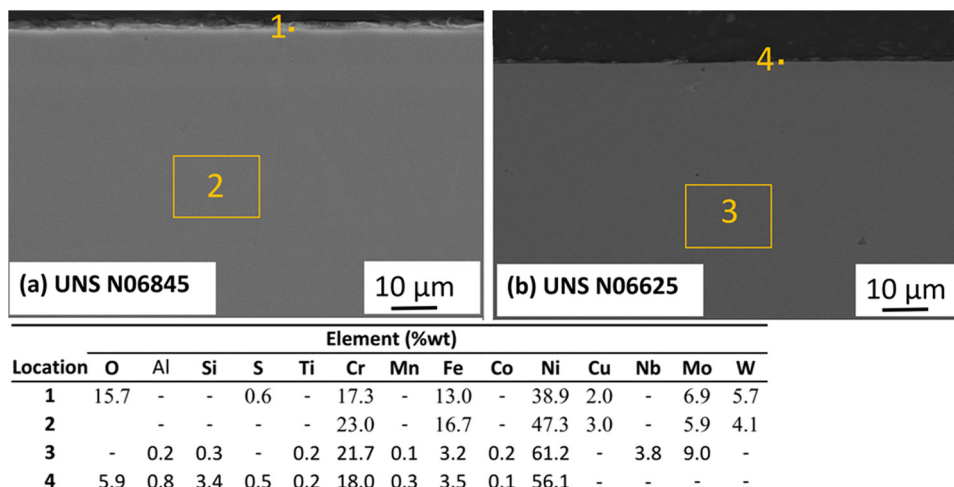

	Element (%wt)												
Location	O	Al	Si	S	Ti	Cr	Mn	Fe	Co	Ni	Cu	Nb	Mo	W
1	15.7	-	-	0.6	-	17.3	-	13.0	-	38.9	2.0	-	6.9	5.7
2	-	-	-	-	-	23.0	-	16.7	-	47.3	3.0	-	5.9	4.1
3	-	0.2	0.3	-	0.2	21.7	0.1	3.2	0.2	61.2	-	3.8	9.0	-
4	5.9	0.8	3.4	0.5	0.2	18.0	0.3	3.5	0.1	56.1	-	-	-	-

Fig. 6. SEM cross section images and XEDS analysis of nickel-based alloys (a) UNS N06845 and (b) UNS N06625 in $H_2S = 150$ mg/kg and $CO_2 = 250$ mg/kg.
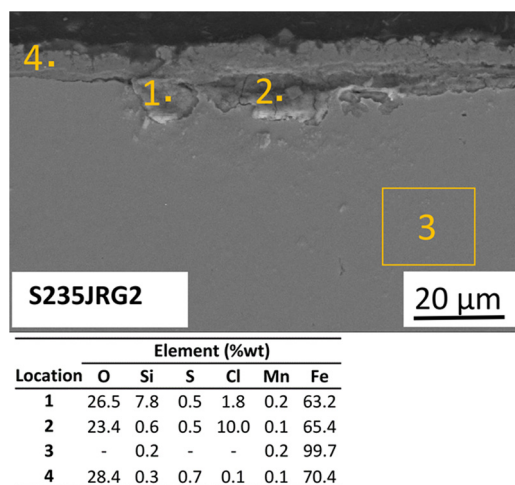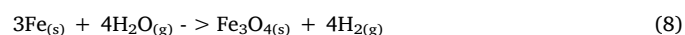
Fig. 8. SEM images and XEDS analysis of a cross section of carbon steel S235JRG2 in H_2S = 150 mg/kg and CO_2 = 250 mg/kg.

magnetite film on the carbon steel S235JRG2 as previously mentioned in Section 3.2. Microething of the cross section of some of the nickel-based alloys after corrosion testing in low concentration of H_2S and CO_2 can be viewed in Fig. 15.

4. Discussion

Factors influencing corrosion behaviour in high temperature aqueous solution and corrosion behaviour in superheated steam were explained by the difference in fluid properties which have a significant effect on the corrosion behaviour. Kritzer [24] and Tjelta [25] conclude that the most important property of H_2O is the density when determining the corrosion rate in superheated or supercritical water. The polarity and solvent property of a superheated fluid are different from the aqueous fluid. In superheated low-density steam, the relatively long distance between the H_2O molecules makes the steam non-polar and a poor solvent for salts and as a result, ionic compounds such as HCl, will not dissociate into ions. The ionic species are the driving force for the conventional electrochemical corrosion in aqueous electrolyte. Kritzer [24] concluded that the corrosion rate is insignificant when the density of superheated steam is below $200 - 300 \, kg/m^3$ in superheated/supercritical environment. Due to lack of polarity and hence electrochemical pathways for the corrosion reactions for low density fluids, a slow radical chemical reaction is more favourable than electrochemical driven reactions. Marroe [26] states that the most severe corrosion in

supercritical water systems is when electrolyte density and concentration of ionic species are high. In the conducted corrosion testing, the density of the superheated fluid was only about $4 \, kg/m^3$ (calculated for pure steam) which is well below the density limit [24] required for the superheated steam to act more like a polar solvent. The density of pure water at a variable temperature at 10 bar gauge can be viewed in Fig. 16. Furthermore, it can be expected that slow radical reactions are preferably occurring but not electrochemical reactions in the testing environment. As a result, radical reactions at the surface of low carbon steel S235JRG2 are likely to have occurred. The difference between the corrosion behaviour of the carbon steel and the more corrosion resistant alloys can be explained by the lack of adherent and sustainable passive film on the low carbon steel S235JRG2. The S235JRG2 lacks chromium and molybdenum to enhance the ability to maintain passive behaviour. It is well known that chromium oxide (Cr_2O_3) film makes a protective film on stainless-steels and nickel-based alloys containing chromium. Molybdenum, which is also a major alloying element in all the corrosion resistant alloys has an ability to enhance the films that provide protective property of nickel-based alloys in corrosive Cl^--H_2S environment [28]. Tomio [28] demonstrated with membrane potential measurements how molybdenum sulphide corrosion film is a cation selective, but in the same paper, it was demonstrated that iron sulphide corrosion film is an anion selective i.e. allowing for instance passage of negative chloride ions through the iron sulphide film. The anion selectivity of iron sulphide film can explain to some extent the reason for chloride enrichment under the sulphide (iron sulphide) layer in S235JRG2 but it should be noted that due to low density of the superheated fluid in the testing, the chloride was from the HCl gas rather than on anionic Cl^- form. However, transportation of liquid microdroplets, enriched with NaCl salt, from preheater to the testing volume should also not be neglected as a possibility. Bornak [29] and Potter [30] reported magnetite formation of iron in oxygen free water/steam environment and addressed also porosity of magnetite film(s). Porous magnetite films have been reported as well in supercritical CO_2 systems at high temperatures and pressures [31]. Magnetite (Fe_3O_4) is a well-known corrosion product on iron. Carbon steel in a superheated environment has been reported with porous magnetite surface films that might promote the under-film corrosion in supercritical CO_2 systems at high temperatures [31]. Magnetite formation on iron surfaces in a boiler system is also well known where it can evolve in water/steam temperatures above 100 °C according to the following reaction [32],

$$3Fe_{(s)} + 4H_2O_{(g)} - > Fe_3O_{4(s)} + 4H_{2(g)} \qquad (8)$$

where it is believed that $Fe(OH)_2$ is an intermediate species in the Fe_3O_4 formation according to [33] with the following reaction
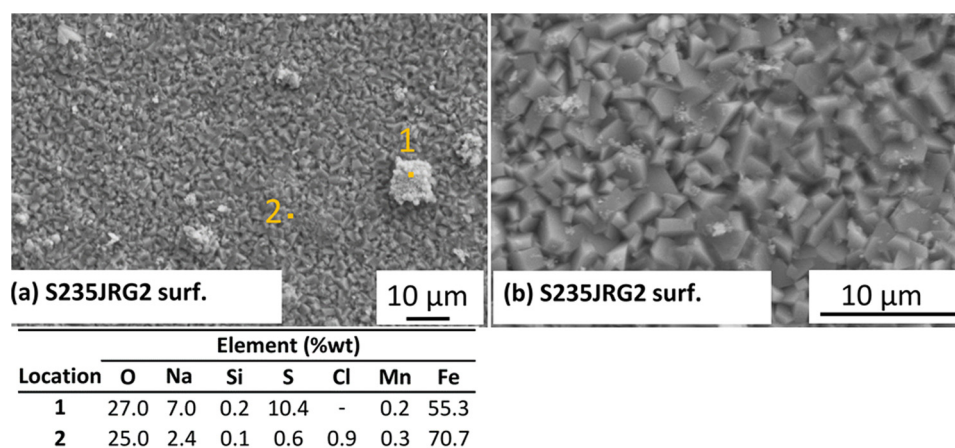

Fig. 9. SEM images and XEDS analysis on external surface of carbon steel S235JRG2 in H_2S = 150 mg/kg and CO_2 = 250 mg/kg at (a) low magnification and (b) at higher magnification.
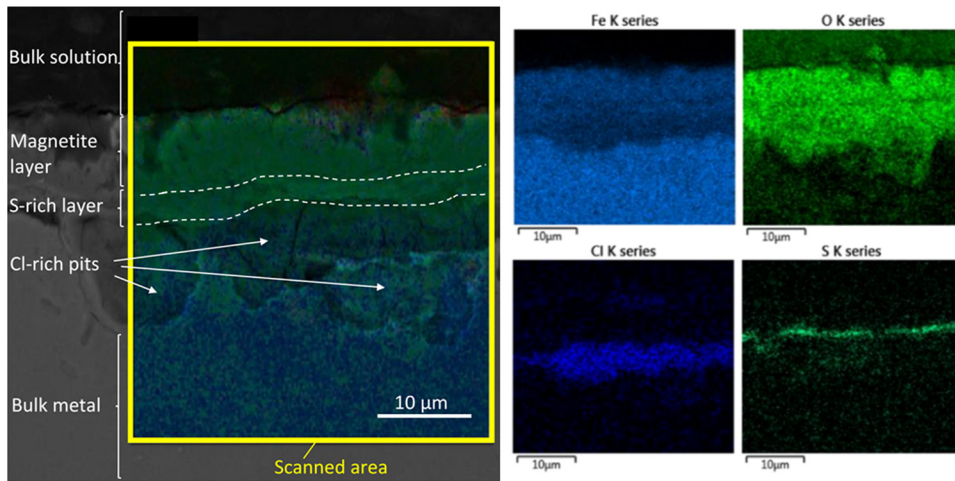
Fig. 10. SEM scanning image (left) of cross section of carbon steel S235JRG2 of oxide layer, sulphur layer and pits profile in the carbon steel in $H_2S = 150\,mg/kg$ and $CO_2 = 250\,mg/kg$. The elemental profile for Fe, O, Cl and S from yellow frame from image (left) can be seen in smaller images at right. (For interpretation of the references to colour in this figure legend, the reader is referred to the web version of this article).

$$3Fe(OH)_{2(s)} - > Fe_3O_{4(s)} + H_{2(g)} + 2H_2O_{(g)} \qquad (9)$$
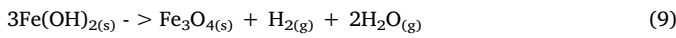
Some oxide, magnetite like and sulphide corrosion products were reported in carbon steel tested in IDDP-1 well [7,9]. Small magnetite formation according to XRD and SEM analysis in the stainless steels in this study implies that steam is oxidizing the iron in the stainless steels alloy but to smaller extend in comparison with the low carbon steel. Chromium oxide passive layer in the stainless-steel alloys could explain the low extend of magnetite formation from iron in the stainless-steel alloys in comparison with the iron in the carbon steel. Corrosion effect of hydrogen sulphide on iron in geothermal systems is quite well known and proposed mechanism of a reaction of H_2S corrosion on Fe has been proposed Banas [34] where the total reaction is

$$Fe + H_2S - > FeS + H_2 \qquad (10)$$

The proposed mechanism for acidic chloride attack and diffusion of chlorides through porous magnetite film in boilers resulting in pitting in an aqueous environment is also described in Strehblow [35] but limited data about pitting behaviour of low carbon steel in superheated H_2S-CO_2-HCl environment is available. Literature [36–42] discussing various reaction mechanism between sulphur or hydrogen sulphide
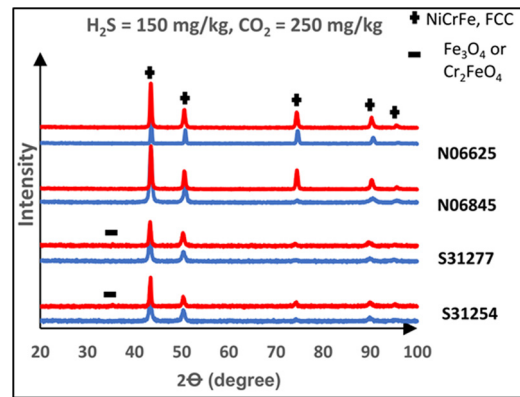

Fig. 12. XRD analysis of corroded (red) and blank (blue) austenitic stainless steels and nickel-based alloys samples in the higher concentration of H_2S/CO_2 testing. (For interpretation of the references to colour in this figure legend, the reader is referred to the web version of this article).
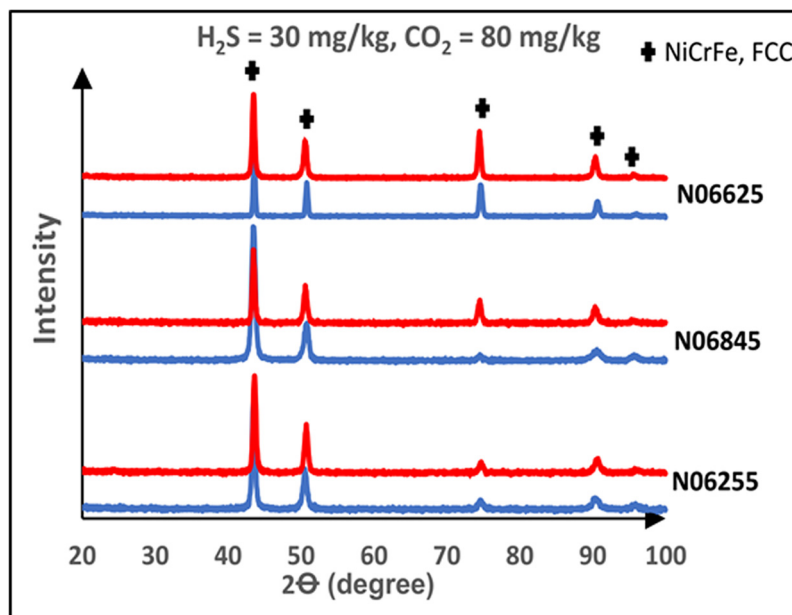

Fig. 11. XRD analysis of corroded (red) and blank (blue) nickel-based samples in the low H_2S/CO_2 concentration testing. (For interpretation of the references to colour in this figure legend, the reader is referred to the web version of this article).
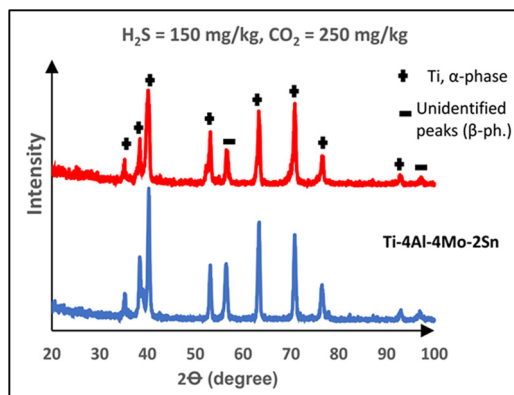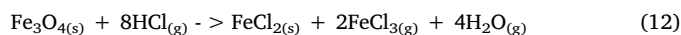
Fig. 13. XRD analysis of corroded (red) and blank (blue) titanium Ti-4Al-4Mo-2Sn samples in the higher concentration of H_2S/CO_2 testing. (For interpretation of the references to colour in this figure legend, the reader is referred to the web version of this article).

vapours with iron shows that corrosion rate, corrosion film structure, integrity and porosity is dependent on several factors including temperature and the composition of the corrosive media. Gao et al. [36] studied formation and propagation mechanism of iron sulphide film on mild steel when the mild steel was tested without oxide film and with preformed $Fe_3O_{4(s)}$ film in a high temperature H_2S environment. The corrosion film mechanism proposes that $Fe_3O_{4(s)}$ forms as an inner layer and $FeS_{(s)}$ forms as an outer layer. Furthermore, the layer growth mechanism in the study indicated that the outer iron sulphide film converts directly from the inner magnetite film. In the carried out testing, the surface of the carbon steel S235JRG2 had chloride enriched pits under inner sulphide corrosion layer and outer magnetite corrosion layer. This layer orientation indicates a different reaction mechanism than experienced in an aqueous environment [36]. The occurrence of inner sulphide layer, outer magnetite layer and chloride rich localized damage under the films in S235JRG2 indicates different corrosion mechanism of low carbon steel is occurring in H_2S-CO_2-HCl environment in comparison with H_2S or H_2S-CO_2 environment. The reaction mechanism of S235JRG2 in our testing could have some similarities with a reaction mechanism proposed by Schmid et al. [43] for stainless

steels in H_2S-CO_2-HCl at 680 °C. Schmid et al. proposed gaseous HCl could penetrate oxides passive film in stainless steels and react with the metallic substrate and form volatile $FeCl_{2(g)}$ that could diffuse outwards the corrosion film towards higher partial pressure of $H_2O_{(g)}$ where they would react and produce HCl and iron oxide. The resulting corrosion film would accommodate chloride enriched sites under iron oxide inner layer and iron sulphide outer layer. In our testing, however, the sulphide layer was the inner layer and magnetite the outer layer. This film layer orientation might be explained by the additional effect of gaseous HCl when it penetrates through the porous/disrupted sulphide and preformed magnetite film and reacts with the iron in the bulk metal or with the inner preformed $Fe_3O_{4(s)}$ layer and forms volatile $FeCl_{3(g)}$ and less volatile $FeCl_{2(s)}$ intermediate corrosion product accumulating at the bulk metal surface. From stoichiometry, the reactions at the bulk iron surface and inner magnetite could be as follows:

$$3Fe_{(s)} + 8HCl_{(g)} -> FeCl_{2(s)} + 2FeCl_{3(g)} + 4H_{2(g)} \tag{11}$$

$$Fe_3O_{4(s)} + 8HCl_{(g)} -> FeCl_{2(s)} + 2FeCl_{3(g)} + 4H_2O_{(g)} \tag{12}$$

The volatile $FeCl_{3(g)}$ corrosion product could then diffuse towards the surface i.e. towards higher partial pressure of $H_2O_{(g)}$ where $FeCl_{3(g)}$ reacts with $H_2O_{(g)}$ and forms magnetite, $Fe_3O_{4(s)}$, other chloride and hydrogen-based corrosion products at the external side of iron sulphide layer. Our testing was conducted at 350 °C and from physical properties of iron chlorides [44,45] it is likely that only $FeCl_{3(g)}$ but not $FeCl_{2(g)}$ would act as a volatile corrosion product and diffuse outwards of corrosion film towards higher partial pressures of $H_2O_{(g)}$ and form outer magnetite layer. The reaction mechanism of $FeCl_{3(g)}$ and $H_2O_{(g)}$ to form $Fe_3O_{4(s)}$ is not straightforward and could be a field of future research. We will therefore simplify our proposed mechanism for the reaction mechanism and evolvement of the corrosion form of the carbon steel S235JRG2 in superheated H_2S-CO_2-HCl environment as illustrated in Fig. 17. In our testing of the carbon steel S235JRG2, some amount of sodium (Na) in the chloride enriched pits were detected in the carbon steel at 350 °C but Simonson et al. [46] have shown that NaCl is present in both vapour and liquid state at 350 °C but potential transportation of NaCl dissolved in microdroplets from boiling in preheater to the reactor (s) should not be neglected. It is also quite well known that inclusions can affect corrosion behaviour of metals and alloys as described by Yang [47]. Inclusions could have served as a weak point or initialisation
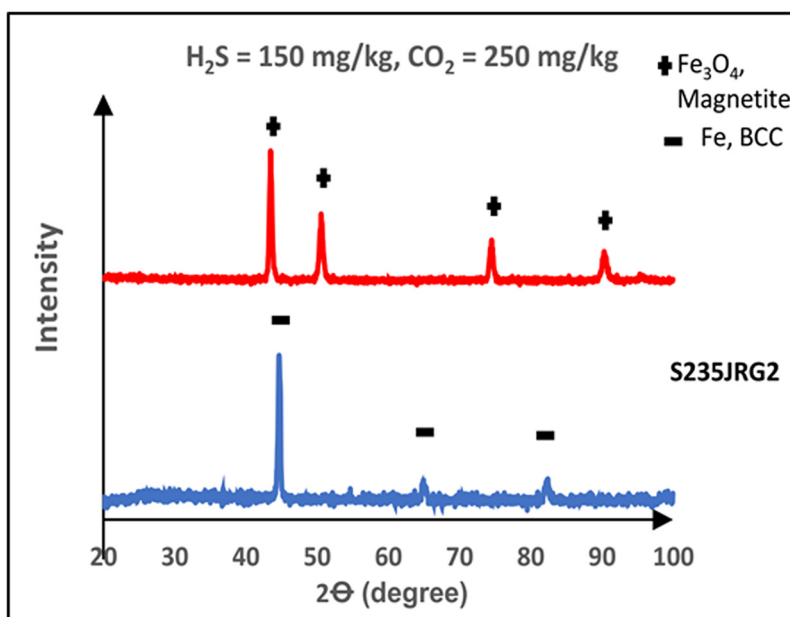

Fig. 14. XRD analysis of corroded (red) and blank (blue) carbon steel S235JRG2 samples in the higher concentration of H_2S/CO_2 testing. (For interpretation of the references to colour in this figure legend, the reader is referred to the web version of this article).
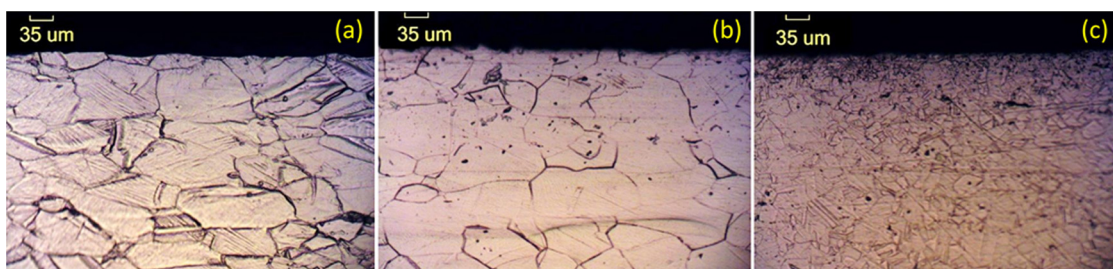
Fig. 15. Etching of (a) UNS N06255, (b) UNS N06845 and (c) UNS N06625 after testing in $H_2S = 30\,mg/kg$ and $CO_2 = 80\,mg/kg$.
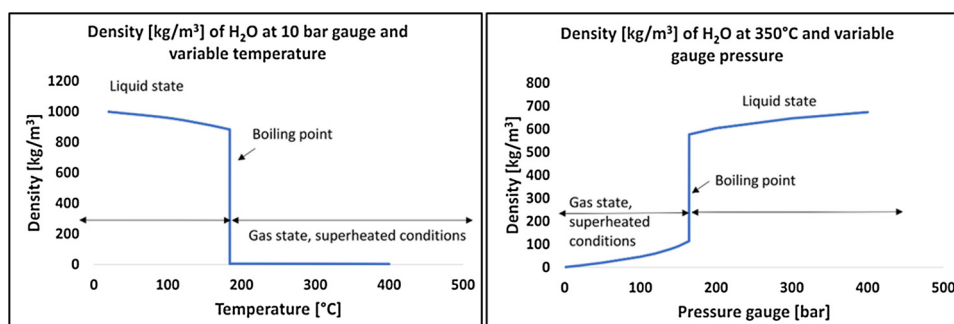

Fig. 16. Density of pure H_2O at 10 bar gauge vs. temperature (left) and density of H_2O at 350 °C vs. gauge pressure (right) with adapted data from [27]. Saturation point of pure water at 10 bar gauge is 184.1 °C and critical temperature of water is at 374 °C.

point for a disruption in the corrosion film, where penetration of $HCl_{(g)}$ through the corrosion film could have occurred and induced the formation of a localized chloride enriched pits in our testing. Oxygen and sulphur rich corrosion products, pitting and localized damage were also observed in carbon steel samples tested in-situ in IDDP-1 well [7,48]. Magnetite has a relatively high electrical conductivity and when magnetite is in contact with carbon steel, it has found to bridge galvanic coupling between the magnetite and the carbon steel. As a result, magnetite film has been reported to accelerate the corrosion rate of carbon steel in a corrosive environment [49]. In our low conductivity corrosive testing fluid, however, the corrosion damage was localized, uniformly distributed at the surface of low carbon steel but more general corrosion damage on the carbon steel would be expected if the galvanic coupling between magnetite and the low carbon steel were inducing corrosion. Corrosion rate experiments in various temperature and pressure indicate that the general corrosion rate below a density of $200\,kg/m^3$ is very low due to the low ionic character of the fluid [50]. The measured corrosion rate in this study is also consistent with the corrosion rate results observed in the field testing conducted in the superheated fluid in the Iceland Deep Drilling Project no. 1 well [7] as seen in Table 5.

5. Conclusions

In low density, superheated, simulated geothermal fluid containing H_2S, CO_2 and HCl at 350° and 10 bars gauge, the general corrosion rate of carbon steel, austenitic stainless steel, nickel-based alloys and the titanium alloy tested is low. No significant corrosion or morphology changes were observed on the nickel-based alloys and titanium alloy. These results imply that these alloys are more resistant to corrosion than the carbon steel and the austenitic stainless steel in the simulated high temperature geothermal environment. Minor morphology changes were observed on the austenitic stainless steels after the testing. The carbon steel, S235JRG2, was the only material tested that was prone to some localized corrosion damage. Chloride rich pits, under the sulphide inner film and magnetite outer film on the carbon steel, could be explained by a penetration of $HCl_{(g)}$ through the corrosion film that reacts with iron and magnetite, forming volatile $FeCl_{3(g)}$ that diffuses

outwards of corrosion film towards higher partial pressures of $H_2O_{(g)}$ where external magnetite layer is formed. No intergranular corrosion was observed in all the materials. All materials tested, except the carbon steel, could be applicable as a construction material in a superheated geothermal environment. From another field testing in the superheated geothermal environment containing H_2S, CO_2, HCl, HF, H_2 and other species, the general corrosion rate was also measured very low, but all the materials tested were however prone to localized corrosion damage. In the current study, localized damage was though only observed in the carbon steel in the simulated high temperature geothermal testing. As the main difference between the reported geothermal field testing and the simulated high temperature geothermal testing is HF and H_2, silica deposition and longer exposure time, it can be concluded that the main reason for localized corrosion damage observed in previous field testing could be due to effect of these additional factors.

Research on the interaction between corrosion and scaling in low temperature geothermal environment has confirmed the protective role of scaling for low grade alloys but limited literature is presently found for this behaviour in superheated geothermal environment. The lower corrosion rate reported in superheated geothermal field in comparison with the testing results presented in the paper might also be due to the protective effect of silica on covering the field samples. Currently, there is an ongoing study by the authors to address this topic by using the current laboratory setup, to study under deposit corrosion behaviour of nickel-based alloys in superheated conditions covered with amorphous silica scale from geothermal field fluid.

Author statement

Andri Isak Thorhallsson: Conceptualization, methodology, experimental/laboratory work and development of laboratory testing facility, experimental analysis; SEM, XEDS, XRD, micro etching of alloys,
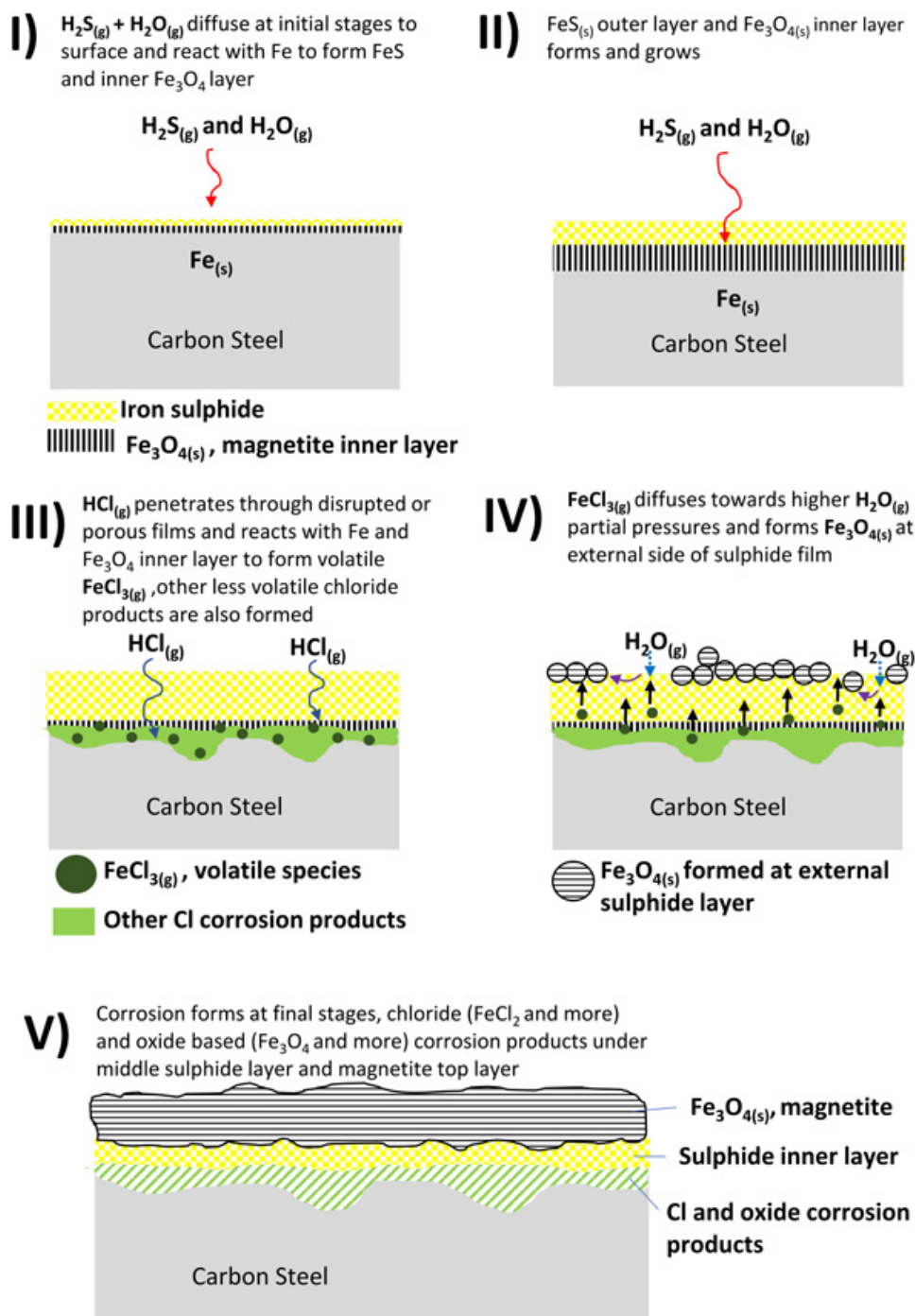
Fig. 17. Proposed mechanism of outer magnetite (Fe₃O₄) film formation, sulphide rich inner layer formation and chloride rich pit formation in carbon steel (S235JRG2) in the simulated geothermal environment.

Table 5
Corrosion rate of few alloys in in-situ testing in Iceland Deep Geothermal Well no.1 – IDDP-1 [5].

Material type	Alloy	Corrosion rate [mm/year]
Low carbon steel	SJ235JRG2	0.004
Austenitic st. steel	UNS S31254	0.001
Nickel based alloy	UNS N06255	0.000
	UNS N06625	0.001
Titanium alloy	UNS R50400	0ᵃ
	UNS R52400	0.011

ᵃ Weight gain detected.

Declaration of Competing Interest

The authors declare that they have no known competing financial interests or personal relationships that could have appeared to

influence the work reported in this paper.

Acknowledgements

Appendix A. Supplementary data

Supplementary material related to this article can be found, in the online version, at doi:https://doi.org/10.1016/j.corsci.2020.108584.

References

[1] S.K. Sanyal, J.W. Morrow, Success and the Learning Curve Effect in Geothermal Well Drilling – A World side Survey, Thirty-Seventh Workshop on Geothermal Reservoir Engineering/2012, Stanford, CA, SGP-TR-194. https://pangea.stanford.edu/ERE/db/IGAstandard/record_detail.php?id=8346.

[2] T. Reinsch, P. Dobson, H. Asanuma, E. Huenges, F. Poletto, B. Sanjuan, Utilizing supercritical geothermal systems: a review of past ventures and ongoing research activities, Geotherm Energy 5 (2017) 16, https://doi.org/10.1186/s40517-017-0075-y.

[3] G.O. Fridleifsson, W.A. Elders, The Iceland Deep Drilling Project: a search for deep unconventional geothermal resources, Geothermics 34 (2005) 269–285, https://doi.org/10.1016/j.geothermics.2004.11.004.

[4] R.O. Fournier, Hydrothermal processes related to moment of fluid from plastic into brittle rock in the magmatic-epithermal environment, Econ. Geol. 94 (1999) 1193–1211, https://doi.org/10.2113/gsecongeo.94.8.1193.

[5] G.O. Fridleifsson, A. Albertsson, W.A. Elders, The iceland deep drilling project (IDDP): planning for the second deep well at Reykjanes, GRC Trans. 35 (2011) 347–354.

[6] T. Hauksson, S. Markusson, K. Einarsson, S.N. Karlsdottir, A. Einarsson, A. Moller, T. Sigmarsson, Pilot testing of handling the fluids from the IDDP-1 exploratory geothermal well, Krafla, N.E. Iceland, Geothermics 49 (2014) 76–82, https://doi.org/10.1016/j.geothermics.2013.07.003.

[7] S.N. Karlsdottir, K.R. Ragnarsdottir, I.O. Thorbjornsson, A. Einarsson, Corrosion testing in superheated geothermal steam in Iceland, Geothermics 53 (2015) 281–290, https://doi.org/10.1016/j.geothermics.2014.06.007.

[8] S.N. Karlsdottir, K.R. Ragnarsdottir, A. Moller, I.O. Thorbjornsson, A. Einarsson, On-site erosion-corrosion testing in superheated geothermal steam, Geothermics 51 (2014) 170–181, https://doi.org/10.1016/j.geothermics.2014.01.007.

[9] S.N. Karlsdottir, I.O. Thorbjornsson, T. Sigmarsson, Corrosion and Scaling in Wet Scrubbing Equipment of the Superheated Geothermal Well IDDP-1 in Iceland, Corrosion/2013, NACE, Orlando, FL, paper no. 2556. https://store.nace.org/corrosion-and-scaling-in-wet-scrubbing-equipment-of-superheated-geothermal-well-iddp-1-in-iceland.

[10] I.O. Thorbjornsson, S.N. Karlsdottir, T. Sigmarsson, Corrosion Testing of Heat Exchanger Tubes in Steam from the IDDP-1 Exploratory Geothermal Well in Krafla Iceland, Corrosion/2014, San Antonio, TX, paper no. 9680. https://store.nace.org/corrosion-testing-of-heat-exchanger-tubes-in-steam-from-the-iddp-1-exploratory-geothermal-well-in-kr.

[11] K. Ingason, V. Kristjánsson, K. Einarsson, Design and development of the discharge system of IDDP-1, Geothermics 49 (2014) 58–65, https://doi.org/10.1016/j.geothermics.2013.05.002.

[12] E.T. Eliasson, A. Einarsson, Corrosion in Icelandic high-temperature geothermal systems, Mater. Perform. Charact. 10 (21) (1982) 35–39.

[13] S.N. Karlsdottir, I.O. Thorbjornsson, Corrosion Testing Down-hole in a Sour High Temperature Geothermal Well in Iceland, Corrosion/2013, NACE, Orlando, FL, paper no. 2550. https://store.nace.org/corrosion-testing-downhole-in-sour-high-temperature-geothermal-well-in-iceland.

[14] W.F. Bogaerts, I. Winstons, Geothermal Corrosion: High-temperature Pitting of Stainless steels and Ni-alloys, Corrosion/2017, NACE, New Orleans, LA, paper no. 9269. https://store.nace.org/geothermal-corrosion-high-temperature-pitting-of-stainless-steels-and-ni-alloys.

[15] A.I. Thorhallsson, S.N. Karlsdottir, A. Stefansson, Corrosion Testing of UNS S31603 in Simulated HT Geothermal Environment at Boiling, Superheated and Condensation Condition, Corrosion/2019, NACE, Nashville, TN, paper no. 13195. https://www.onepetro.com/conference-paper/NACE-2019-13195.

[16] A.I. Thorhallsson, S.N. Karlsdottir, A. Stefansson, Corrosion Testing of UNS N06625 in Simulated High Temperature Geothermal Environment, Corrosion/2018, NACE, Phoenix, AZ, paper no. 11058. https://store.nace.org/corrosion-behavior-of-austenitic-stainless-steels-and-nickel-alloys-in-simulated-ht-geth-environm-2.

[17] S. Arnorsson, Isotopic and Chemical Techniques in Geothermal Exploration, Development and Use: Sampling Methods, Data Handling, Interpretation, International Atomic Energy Agency, Vienna, 2000, pp. 114–115 https://www.iaea.org/publications/5733/isotopic-and-chemical-techniques-in-geothermal-exploration-development-and-use-sampling-methods-data-handling-interpretation-edited-by-stefan-arnorsson.

[18] S. Arnorsson, J.O. Bjarnason, N. Giroud, I. Gunnarsson, A. Stefansson, Sampling and analysis of geothermal fluids, Geofluids 6 (2006) 203–216, https://doi.org/10.1111/j.1468-8123.2006.00147.x.

[19] S. Arnorsson, Isotopic and Chemical Techniques in Geothermal Exploration, Development and Use: Sampling Methods, Data Handling, Interpretation, International Atomic Energy Agency, Vienna, 2000, pp. 108–113 https://www.iaea.org/publications/5733/isotopic-and-chemical-techniques-in-geothermal-exploration-development-and-use-sampling-methods-data-handling-interpretation-edited-by-stefan-arnorsson.

[20] ASTM International, ASTM G1-90: Standard Practice for Preparing, Cleaning, and Evaluating Corrosion Test Specimens, (2017), p. 3 https://www.astm.org/Standards/G1.

[21] G. Petzow, Metallographic Etching, American Society for Metals, Ohio, USA, 1978, p. 64.

[22] G. Petzow, Metallographic Etching, American Society for Metals, Ohio, USA, 1978, p. 87.

[23] G.F. Vander Voort, J.W. Bowman, R.B. Frank, Microstructural characterization of custom age 625 plus alloy, The Minerals, Metals & Materials Society (1994) 489–498 https://www.researchgate.net/publication/269258305_Microstructural_Characterization_of_Custom_Age_625_Plus_Alloy.

[24] Peter Kritzer, Corrosion in high-temperature and supercritical water and aqueous solutions: a review, J. Supercrit. Fluids 29 (2004) 1–29, https://doi.org/10.1016/S0896-8446(03)00031-7.

[25] M. Tjelta, B.C. Krogh, S. Sæther, M. Seiersten, Corrosion, Scaling and Material Selection in Deep Geothermal Wells - Application to IDDP-2, Corrosion/2019, paper no. 13299 NACE, Nashville, TN, 2019 https://store.nace.org/corrosion-scaling-and-material-selection-in-deep-geothermal-wells-a-case-study-of-iddp-2-63025.

[26] P.A. Marroe, G.T. Hong, Corrosion control methods in supercritical water oxidation and gasification processes, J. Supercrit. Fluids 51 (2009) 83–103, https://doi.org/10.1016/j.supflu.2009.08.001.

[27] Wolfram Alpha LLC, Wolfram Alpha Widgets, (2019) (Accessed 7 August 2019), https://www.wolframalpha.com/widgets/view.jsp?id=1de7d2b90d554be9f0db1c338e80197d.

[28] A. Tomio, M. Sagara, T. Doi, H. Amaya, N. Otsuka, T. Kudo, Role of alloyed molybdenum on corrosion resistance of austenitic Ni-Cr-Mo-Fe alloys in H_2S-Cl^- environments, Corros. Sci. 98 (2015) 391–398.

[29] W.E. Bornak, Chemistry of Iron and its corrosion products in boiler systems, Corrosion 44 (3) (1988) 154–158, https://doi.org/10.1016/j.corsci.2015.05.053.

[30] E.C. Potter, G.M.W. Mann, The fast linear growth of magnetite on mild steel in high-temperature aqueous conditions, Br. Corros. J. 1 (1) (1965) 26–35, https://doi.org/10.1179/000705965798328182.

[31] V. Firouzdor, K. Sridharan, G. Cao, M. Anderson, T.R. Allen, Corrosion of a stainless steel and nickel-based alloys in high temperature supercritical carbon dioxide environment, Corros. Sci. 69 (2013) 281–291, https://doi.org/10.1016/j.corsci.2012.11.041.

[32] F.A. Cotton, G. Wilkinson, Advanced Inorganic Chemistry, 4th edition, Wiley-Interscience, New York, New York, 1980, pp. 752–766.

[33] U.R. Evans, J.N. Wanklyn, Evolution of hydrogen from ferrous hydroxide, Nature 162 (1948) 27, https://doi.org/10.1038/162027b0.

[34] J. Banas, U. Lelek-Borkowska, B. Mazurkiewics, W. Solarski, Effect of CO_2 and H_2S on the composition and stability of passive film on iron alloys in geothermal water, Electrochm. Acta 52 (2007) 5704–5714, https://doi.org/10.1016/j.electacta.2007.01.086.

[35] H.H. Strehblow, Mechanism of pitting corrosion, in: P. Marcus (Ed.), Corrosion Mechanisms in Theory and Practice, CRC Press, Boca Raton, 2012, p. 370.

[36] S. Gao, B. Brown, D. Young, S. Nesic, M. Singer, Formation Mechanism of Iron Oxide and Iron Sulfide at High Temperature in H2S Corrosion Environment, Corrosion/2018, NACE, Phoenix, AZ, paper no. 11027. https://store.nace.org/formation-mechanisms-of-iron-oxide-and-iron-sulfide-at-high-temperature-in-h2s-corrosion-environment-2.

[37] Z.A. Foroulis, Kinetics and mechanism of the reaction of iron with sulfur vapor in the temperature range of 250 to 500°C, Werkst. Und Korrosion 29 (1978) 385–393, https://doi.org/10.1002/maco.19780290602.

[38] H. Ma, X. Cheng, G. Li, S. Chen, Z. Quan, S. Zhao, L. Niu, The influence of hydrogen sulfide on corrosion of iron under different conditions, Corros. Sci. 42 (2000) 1669–1683, https://doi.org/10.1016/S0010-938X(00)00003-2.

[39] W. Sun, S. Nesic, S. Papavinasam, Kinetics of corrosion layer formation. Part 2 – iron sulfide and mixed Iron sulfide/carbonate layers in carbon Dioxide/Hydrogen sulfide corrosion, Corrosion 64 (no.7) (2008) 586–599, https://doi.org/10.5006/1.3278494.

[40] S. Ramachandran, M.B. Ward, K.A. Bartrip, Molecular Modelling of Corrosion of Iron in H2S Environments, Corrosion/2002, Denver, CO, paper no. 02240. https://store.nace.org/02240-molecular-modeling-of-corrosion-of-iron-.

[41] R.C. John, A.L. Young, New Understanding on Corrosion of Alloys in High-Temperature Sulfidizing Gases, Corrosion/2002, Denver, CO, paper no. 02486. https://store.nace.org/02486-new-understanding-on-corrosion-of-.

[42] N.A.C.E. International, Task Group (TG) 176, Overview of Sulfidation (Sulfidic) Corrosion in Petroleum Refining Hydroprocessing Units, NACE International Publication, 2014, p. 34103 https://store.nace.org/nace-publication-34103-2014-.

[43] A. Schmid, G. Mori, E. Bucher, R. Haubner, Model about the course of corrosion reactions of austenitic steels in H2S-, HCl- and CO2-Containing atmospheres at 680°C, Oxid. Met. 91 (2019) 1–10, https://doi.org/10.1007/s11085-018-9876-z.

[44] Pierre R. Roberge, Handbook of Corrosion Engineering, second ed., McGraw-Hill,

USA, 2012, p. 218.

[45] Michael Schütze, High-temperature corrosion, in: P. Marcus (Ed.), Corrosion Mechanisms in Theory and Practice, CRC Press, Boca Raton, 2012, p. 575.

[46] J.M. Simonson, D.A. Palmer, R.W. Carter, Liquid-Vapor Partitioning of NaCl(aq) from Concentrated Brines at Temperatures to 350°C, Nineteenth Workshop on Geothermal Reservoir Engineering/1994, Stanford, CA. https://www.osti.gov/servlets/purl/10126322.

[47] S. Yang, M. Zhao, J. Feng, J. Li, C. Liu, Induced-pitting behaviors of MnS inclusions in steel, High Temp. Mater. Process. 37 (9-10) (2018) 1007–1016, https://doi.org/10.1515/htmp-2017-0155.

[48] K.R. Ragnarsdottir, Corrosion Experiments in Dry Superheated Steam From IDDP-1, M.SC. Thesis, University of Iceland, Faculty of Industrial Engineering, Mechanical Engineering and Computer Science, 2013, http://hdl.handle.net/1946/13893.

[49] G.D. Song, S.-H. Jeon, Y.-H. Son, J.G. Kim, D.H. Hur, Galvanic effect of magnetite on the corrosion behavior of carbon steel in deaerated alkaline solutions under flowing conditions, Corros. Sci. 131 (2018) 71–80, https://doi.org/10.1016/j.corsci.2017.10.017.

[50] P. Kritzer, N. Boukis, E. Dinjus, Review of the corrosion of nickel-base alloys and stainless steels in strongly oxidizing pressurized high-temperature solutions at sub- and supercritical temperatures, Corrosion 56 (2000) 1093, https://doi.org/10.5006/1.3294394.